A TIP-TILT-PISTON MICROMIRROR WITH ELASTOMERIC UNIVERSAL JOINT FABRICATED VIA MICRO-MASONRY

BY

ZINING YANG

THESIS

Submitted in partial fulfillment of the requirements
for the degree of Master of Science in Mechanical Engineering
in the Graduate College of the
University of Illinois at Urbana-Champaign, 2014

Urbana, Illinois

Advisor:

Assistant Professor Seok Kim

Abstract

This thesis presents the design, analytical and numerical modeling, fabrication and characterization of a hybrid tip-tilt-piston micromirror driven by electrostatic actuation. The micromirror involves a single crystal silicon mirror and a conductive elastomeric universal joint which are mechanically bonded and electrically interconnected. This device takes advantage of two distinct materials to achieve a high quality reflective surface using single crystal silicon and a highly flexible joint using an elastomer. To realize this hybrid system, micro-masonry techniques are employed such that silicon and elastomer parts are fabricated separately and integrated afterwards. The static and dynamic behaviors of the micromirror are characterized, indicating identical response about its two orthogonal scanning axes. Furthermore, the piston stroke utilized by the compressive deformation of the elastomeric joint along z-axis is investigated.

Acknowledgements

I would like to thank my advisor, Professor Seok Kim, for giving me the opportunity to work on this interesting project. I also thank him for his continuous support and inspiring advice on my research. We collaborate with Prof. Alexander Vakakis's group and I thank him for bringing insight to my work. I also want to thank Professor Placid Ferreira for bringing insight and experience in the discussion of my work at our transfer printing meetings.

Furthermore, I would like to thank my close colleagues and friends here: Dr. Bongwon Jeong, Dr. Yong Zhang, Jeffrey Eisenhaure, Hohyun Keum, and Sangil Rhee. Dr. Bongwon Jeong is my main collaborator in the project and he contributes to the dynamic modeling and characterization for the device. I thank him for his kind help and for his passion in this work. I thank Dr. Yong Zhang because he served as my mentor on research when I first joined the group. I would also thank our current group members Hohyun Keum, Sangil Rhee and Jeffrey Eisenhaure not only for their technical help in preparing samples every now and then, but also their constant advice since I joined the group.

Last but not least, I would like to thank my parents and my girlfriend Weiting for their unconditional support to my life.

Table of Contents

Chapter 1: Introduction

1.1 Micromirror Applications – A Review

Microelectromechanical systems (MEMS) technology-based micromirrors have brought impacts to many areas such as projection displays, optical fiber telecommunications, adaptive optics and biomedical imaging [1]. Among all these applications, projection display has become one of the largest markets for MEMS industry [1]. The early investigations starting from the 1970s ultimately lead to the invention of one of the most well-known MEMS system so far - the Digital Light Processing Technology (DLP) utilizing Digital Mirror Device (DMD) as its core [2]. The DMD system consists of a two-dimensional array of pixels on a silicon substrate. Each pixel consists of an aluminum reflective micromirror supported on a post, which is in turn supported on a platform – the yoke. The yoke is then suspended by two flexure springs anchored on stationary posts [2]. Figure 1 (A) shows the scanning electron microscopy (SEM) image of the micromirror structure without the mirror [2]. Each pixel works as a one degree-of-freedom (1DOF) bistable mirror with tilting angle limited to $\pm 10°$ corresponding to the dark and bright state of a pixel, respectively. The 16-μm-wide mirrors form two-dimensional arrays consist from 800×600 pixels up to 1280×1024 pixels with a 17 μm pitch [1]. The fill factor, defined as the ratio of mirror area to pitch area, is approximately 90% for the DMDs [1]. Surface micromachining is used to fabricate the DMD, which involves thin film patterning and sacrificial layer etching.

Another area that benefit from MEMS technology is the optical fiber telecommunication. Common applications include optical cross-connections (OCX), dynamic gain equalizers, wavelength add–drop multiplexers (WADM) and wavelength-selective switches (WSS) [3]. Figure 1 (D) shows the SEM image of a two-dimensional (2DOF) micromirror developed for WSS applications. Each micromirror acts an optical switch to route signals between optical fibers. The micromirrors form a 1×N linear array which corresponds to 1×N^2 ports. The 100 μm polycrystalline silicon (ploy-Si) micromirror is fabricated through SUMMiT-V process, a five layers surface micromachining process developed by Sandia National Lab [3].

Besides the two aforementioned areas, MEMS mirrors also find applications in biomedical imaging and adaptive optics [3]. Taking biomedical imaging as an example, a key component for optical coherent tomography (OCT) endoscope is the miniature measurement head which utilizing a 2-D micromirror at the optical scanner [4]. To endoscopically place the miniature measurement head into human body, the overall size of it has to be smaller than 5 mm. Two-axis MEMS scanner with the size ~1 mm fulfills the stringent size requirement of the measurement head and provides large scanning angle at the same time (shown in Figure 1 (B)). In adaptive optics, tip-tilt-piston micromirror (Figure. 1 (C)) arrays are used to compensate wavefront distortions generated by the medium [5]. The name "tip-tilt-piston" indicates that every single mirror has 3DOFs including the two rotational axes (tip/tilt) and a vertical linear motion (piston). For the two-axis scanner and the tip-tilt-piston mirror demonstrated in Figure 1, bulk micromachining process is used to generate the free-standing structures.

It can be seen from Figure 1 that common silicon-based MEMS mirrors essentially adopt similar designs with optical reflectors suspended on silicon torsional springs, regardless of their specific applications. To realize such structures, monolithic microfabrication process including surface micromachining and bulk micromachining are generally used. Since one of the main purposes of this thesis is to propose a new fabrication approach to realized new design and material selection form micromirror devices, a digest of the typical microfabrication process is necessary before we can introduce our own approach. We will introduce microfabrication technologies in chapter 1.2, with a concentration on those that are important for the micromirror devices. The general idea of our fabrication routine termed “micro-masonry” will be introduced in chapter 1.3.

1.2 Micromirror Fabrication Techniques

We mentioned in chapter 1.1 that conventional monolithic microfabrication process including surface micromachining and bulk micromachining are generally used to fabricate micromirror devices. Next, we will briefly introduce these two common routines.

As the name suggest, surface micromachining methods refer to the process that creates structures near the surface of the substrate. Since it often involves repeated deposition and patterning of thin films on a wafer scale, the complexity of the whole process is sometimes characterized by the number of structure layers. Because a full digest of the different surface micromachining techniques is somewhat difficult, we show in Figure 2 a representative MEMS foundry process - SUMMiT-V process developed by Sandia National Lab – as an example [6]. As the name suggests, SUMMiT-V is a five layers process utilizing poly-Si as the structural layer and silicon dioxide as the sacrificial layer. Each layer is photolithographic patterned and the sacrificial layers are eventually removed to free the movable structure. Although dimensional structures such as the micromirror device shown in Figure 1 (D) can be fabricated through this process, there are some disadvantages for the surface micromachining methods:

(1) To perform photolithography process for multiple times, the oxide directly beneath the upper two levels of mechanical poly-Si(shown in Figure 1 (B)) have to be planarized using

chemical mechanical polishing (CMP) process to alleviate photolithographic issues caused by the nonflat underlying topography. However, the CMP process is an expensive and time-consuming process that we generally want to avoid.

(2) The material of the mirror is limited to poly-Si, which generally exhibits low qualities than the single crystalline bulk silicon: a rougher surface resulted from the thin film deposition process and a larger curvature as a result of the thermal residual stress.

(3) The thickness of each layer has to be within the limit of thin film deposition techniques, which is in general less than 5 μm. On the other hand, micromirrors for laser scanning applications with mirror size of ~ 1 mm usually require the mirror thickness to be at least 10 μm to maintain its flatness. Apparently the surface micromachining does not satisfy the thickness requirement of large micromirrors, which partly explained why this fabrication routine is often seen for small micromirrors (size < 100 μm).

Bulk micromachining, on the other hand, resolves some of issues of surface micromachining. Figure 3 shows a MEMS foundry process named SOI-MUMPs which well represents the simplest routine of bulk micromachining [7]. Silicon-on-insulator (SOI) wafers with a doped device layer of 10 μm that is isolated from the 400-μm-thick handle layer silicon by a 1 μm buried oxide layer (BOX) is used as the starting material. Both sides of the wafer are etched to create microstructures and the device layers are eventually released by removing the buried-oxide layer. More realistic and complicated design often involves thinning of handle layers via CMP if the thickness of the handle layer also matters. Wafer bonding is usually performed if multiply device layers are needed. Compared with surface micromachining, the bulk micromachining process shows some advantages for MEMS micromirror applications:

since polished single crystal silicon (SCS) is used as the mirror material, it gives high quality reflective surface. The thickness of the mirror is also less constrained compared to surface micromachined device, since SOI wafers with device layer varying from 1 μm to 100 μm are commercially available. The layer-by-layer thin film processing of surface micromachining can be avoided in the bulk micromachining process. However, the process is still quite complex when it comes to the fabrication of three dimensional microstructures due to the presence of wafer thinning and wafer bonding process.

Besides the aforementioned limitations aroused from the microfabrication process, the micromirror utilizing conventional springs design and monolithic fabrication approaches exhibit several other fundamental challenges from material, fabrication and design perspectives.

- Material wise, the structure material for the monolithic micromirrors are generally constrained to SCS or poly-Si. As a well-known brittle material at room temperature, silicon is susceptible to cleavage fracture under large deformation. For micromirrors working under resonant state, rigid silicon hinges suffer from fatigue fracture as a result of the cyclic loading.

- Extremely slender springs with cross-section-width of the order of a few micrometers are usually necessary for monolithic micromirrors in order to obtain a reasonable low stiffness due to the high elastic modulus of silicon (E ~ 170GPa for single crystal silicon). This gives rise to fabrication concerns such as the sensitivity to fabrication error and contamination. For example, the resolution of photolithography process is in the order of μm in common cleanroom facilities. While this is acceptable for some MEMS device, it becomes a real concern when it comes to fine structures such as 5-μm-wide springs, whose dimensions are in the same order of the photolithographic resolution. Besides the photolithography concern, dry etching step often involves undercuts effect (reactive ion etching, or RIE) and scalloping effect (deep reactive ion etching, or DRIE) which will also generate some error in the final product. The final wafer dicing and packaging step involves particle generation and slender springs are extremely susceptible to damage during these processes. All these aforementioned fabrication errors and contamination damages will accumulate and lead to either inconsistent device performance or decrease of the manufacturing yield.

- From design perspective, complex mechanical designs are required to realize a multi-axis micromirror. As a predominant design, a gimbaled structure provides an additional degree of freedom to enable two-axis motion, but it suffers from limitations such as large footprint and unequal frequency responses with respect to the two axes. Gimbaless structures with two or more degrees of freedom are also investigated but they usually require even more sophisticated design and fabrication processes.

To address the aforementioned challenges, this thesis reports a hybrid two-axis micromirror utilizing an elastomeric universal joint where its mechanical deflection occurs. Compared with the silicon springs, the elastomeric joint structures have several advantages: (1) Elastomeric material can sustain enormous deformation (stretch ~ 100%). The reliability can be improved with such soft materials. (2) Due to the low Young’s modulus of elastomers (E ~ 1 MPa), beams with cross section width in the order of tens of micrometers can be used. Though fabrication error still exists, it is less of problem for large features. (3) Three-dimensional motion such as tip-tilt-piston can be realized with a simple and compact gimbaless design.

1.3 Micro-Masonry Techniques

Despite of all the advantages of elastomer-silicon hybrid structures, the fabrication of such device has historically been challenging. Although the fabrication of various hybrid MEMS devices involving elastomer parts have been demonstrated previously [8], such devices not only with mechanical bonding but also with electrical interconnection between elastomer and silicon components have been difficult to realize.

Frequently used elastomer materials in MEMS field are polydimethylsiloxane (PDMS) and polyurethane [9]. Among the two materials, PDMS elastomer has been extensively used in microfluidic application as channels, pumps and valves due to its easiness of fabrication: it can be cast at room temperature and then thermally annealed. After the annealing, PDMS device would replicate the structures on the surface of the mold. When mixed with conductive inclusions, conductive PDMS nanocomposite can be used as materials for conductors, sensors and actuators in the MEMS field [9]. The high electrical conductivity and extremely low Young’s modulus make the conductive PDMS nanocomposite a perfect choice as the material for deformable component in micromirror. However, PDMS nanocomposite is processed either by molding, similar to the pure PDMS, or by screen printing [9]. Hence, the fabrication process is inherently incompatible with the micromachining process described in chapter 1.2.

The incompatibility of material processing for conductive PDMS and silicon indicates that instead of utilizing the monolithic micromachining process where all the materials have to experience the same processes, the PDMS and silicon component needs to be prepared separately and then combined together to form a heterogeneous system. To accomplish such a task, a deterministic microassembling method has to be developed. Previously, our group have proposed a fabrication technique term “micro-masonry” which involves preparation of different components on separate substrate and deterministic assembling of these components to form a desired structure (Figure 4) [10]. The basic units of the final microsystem are prepared in separate substrates called donor substrates. Then, these parts are picked up by an elastomer stamp and printed to another substrate called receiver substrate. This sequence of manipulations is called transfer printing. The final microstructures are formed by repeating this transfer printing process and binding the parts together thermally. Figure 5 shows some of the microstructures and devices that are fabricated by micro-masonry process with silicon components. As demonstrations of the micro-masonry technique, a silicon bricks stack and a silicon teapot are fabricated. To expand the silicon micro-masonry technique to practical MEMS device, a comb-drive capacitor acting as a sensor as well as an actuator is also fabricated and the devices performance is characterized [11]. For the silicon-based micro-masonry, silicon units which later form silicon bricks, silicon rings and the comb drives are prefabricated on SOI donor substrates as transfer-printable units, which are also termed inks. An elastomer stamp with pyramidal shape surface relief is then used to pick up the inks from the donor substrates and then print them on the receiver substrate. Thermal annealing at 1000 ˚C is performed to bind the silicon components together through the activation of silicon fusion bonding. Similarly in this thesis, the silicon later functioning as mirrors and electrodes are fabricated with a process similar to that developed for previous work. At the same time, conductive elastomer structures are formed by selectively doping and subsequent molding in a way similar to what are used for microfluidics fabrications. The silicon and elastomer components are eventually combined together using transfer printing and thermal annealing. Such a fabrication routine eliminates the chance of elastomer to experience harsh microfabrication conditions, such as high temperatur, ion bombardment, and corrosive wet environment. Therefore it enables a strong mechanical and electrical connection between two heterogeneous materials without causing the damage of elastomer.

1.4 Overview

The main purpose of the thesis is to develop a hybrid micromirror utilizing the micro-masonry process described above. The design and modeling of the device is presented in chapter 2, which include both analytical modeling as well as numerical study. The fabrication process is described in chapter 3 in detail. The performance of the micromirror is characterized, with the results shown in chapter 4. We characterized both the static and dynamic behavior of the micromirror system. Furthermore, the mechanical and the electrical properties of the elastomer universal joint are also studied.

1.5 Figures

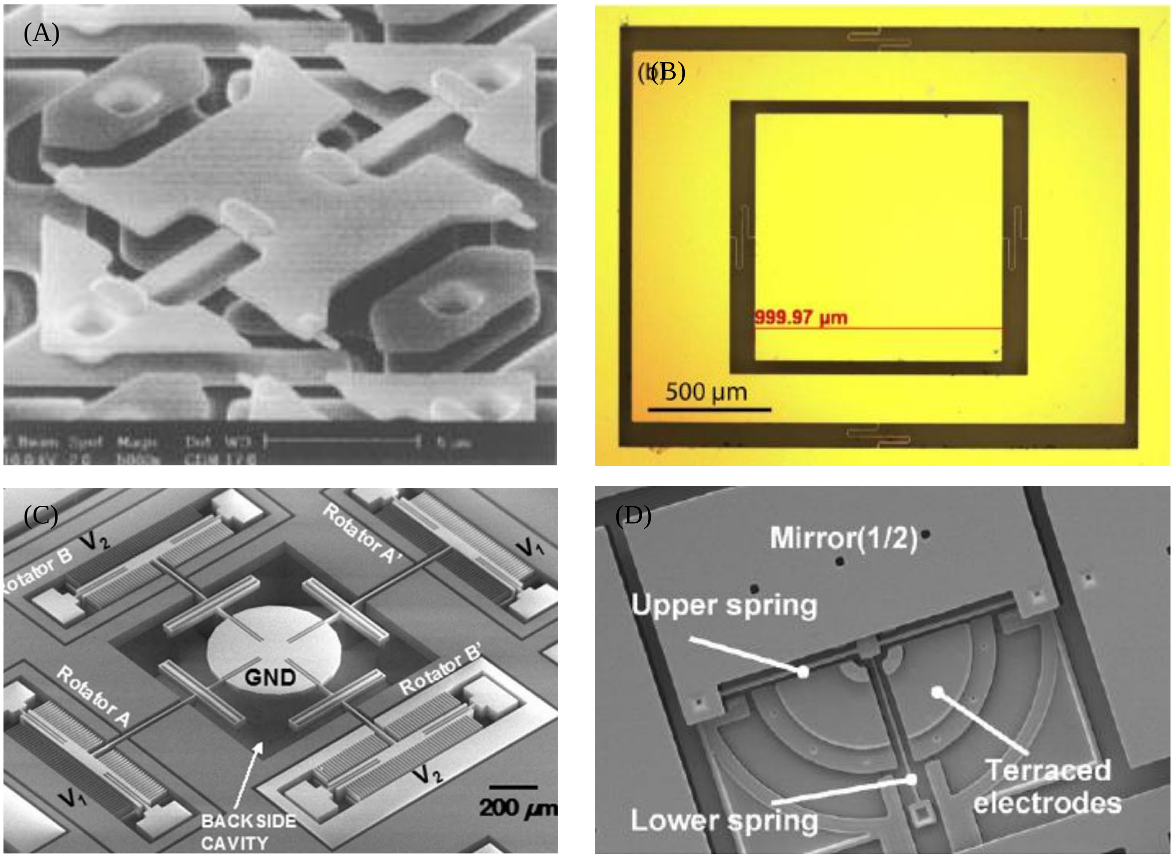

Figure 1. MEMS micromirrors with different applications: (A) SEM image showing the yoke and hinges of a Texas Instrument Digital Micromirror Device (DMD) [2]; (B) top view of a 2D microscanner used for endoscopic optical coherence tomography [4]; (C) SEM image of a tip-tilt-piston micromirror for adaptive optics application [5]; (D) a two-axis scanner for wavelength selective switches applications [3].

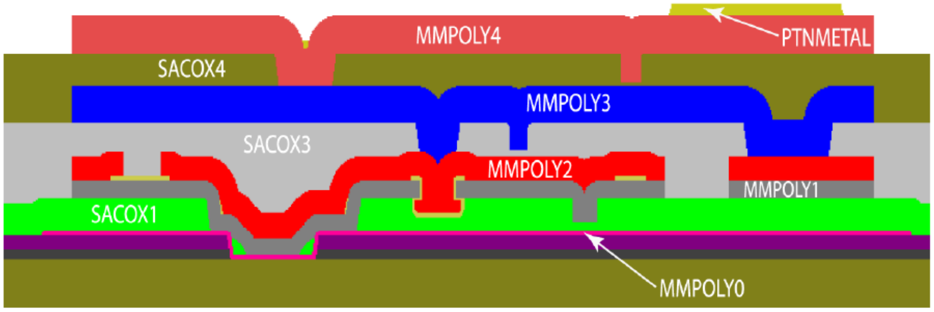

Figure 2. Schematic diagram showing a representative surface micromachining process (SUMMiT-V) [6].

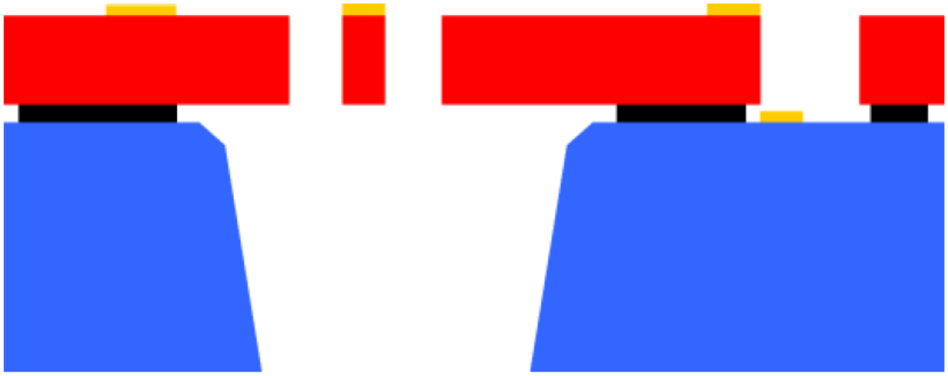

Figure 3. Schematic diagram showing a representative bulk micromachining process (SOI-MUMPs) [7].

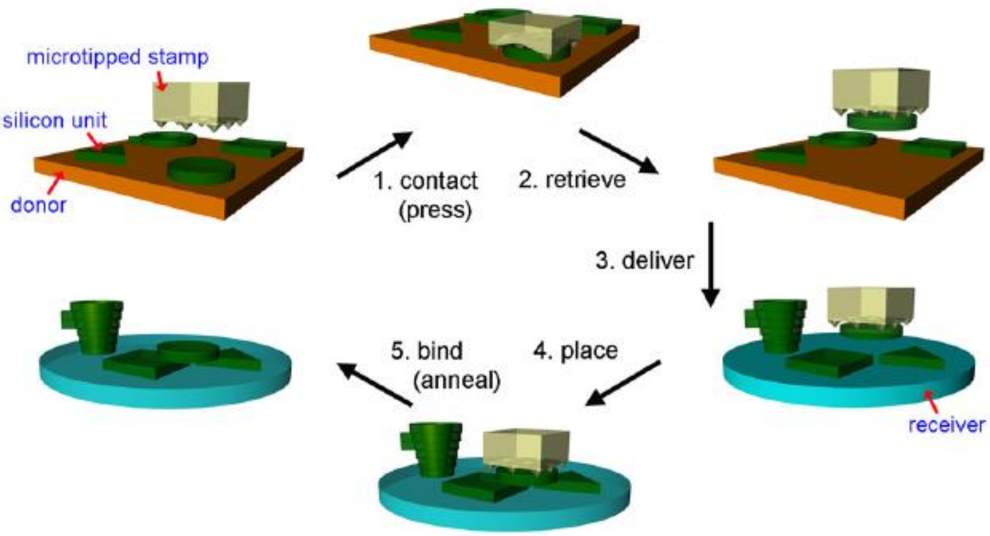

Figure 4. Schematic diagram of the Si micro-masonry process [10].

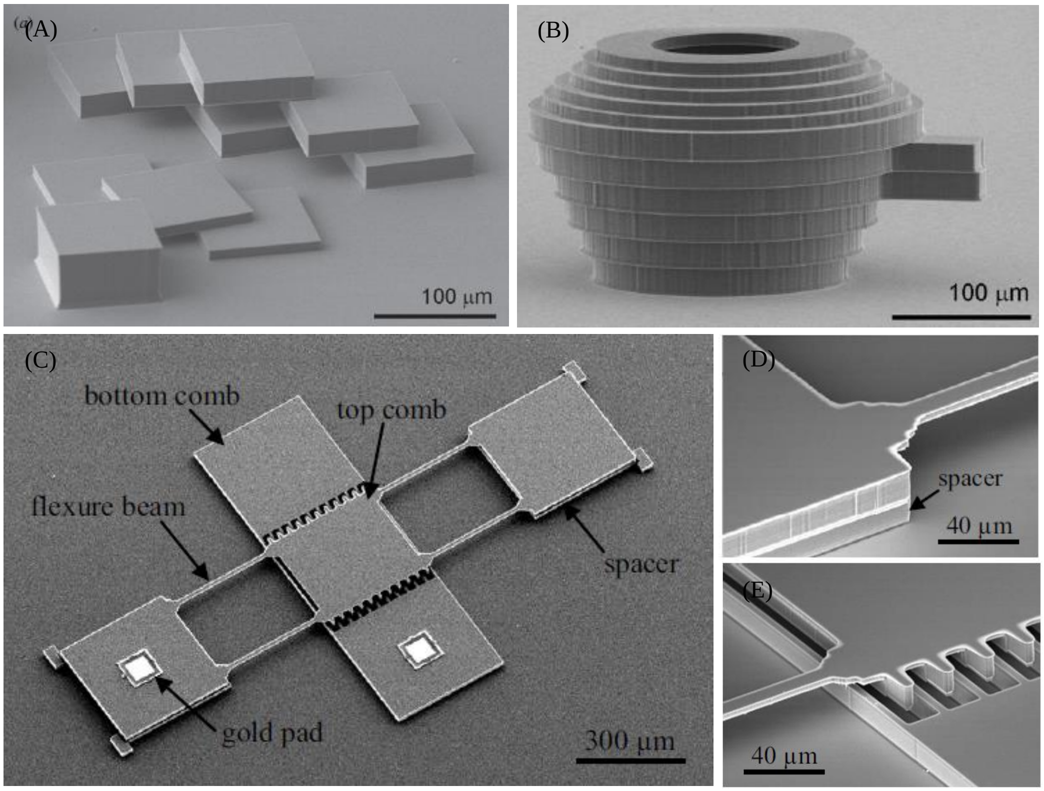

Figure 5. Structures and devices made by silicon micro-masonry: (A) silicon bricks [10], (B) silicon teapot [10], (C) comb-drive device [11], (D, E) closed view of the comb drive device [11].

Chapter 2: Design and Modeling

2.1 Design of the Micromirror

Figure 6 is the schematic diagram of the micromirror that is composed of three key components: an elastomeric universal joint (along with the substrate), a top mirror, and four bottom electrodes. We term the elastomeric cylindrical structure ‘universal joint’ in a sense that it allows bending toward any direction. The mirror and electrodes are made of highly doped single crystal silicon (Ultrasil Corporation) with minimal resistivity (ρ=0.001Ω-cm). Polydimethylsiloxane (PDMS, Sylard 184, Dow Corning) is chosen as the elastomer material due to its excellent mechanical properties and well established processes. To obtain electrical interconnection and isolation, carbon black (CB) particles (VULCAN XC72R, Cabot Corporation) are embedded at selective regions of the PDMS structures including the universal joint and the bases underneath the electrodes. Therefore, the mirror is mechanically and electrically connected to the top surface of the universal joint such that the top mirror and bottom electrodes form a parallel-plate electrostatic actuator.

Upon application of voltage bias between the mirror and one or more of the electrodes, electrostatic traction will create a torque towards the universal joint. The bending deformation occurs at the universal joint will result in the angular deflection of the mirror. If all four of the electrodes are applied with the same voltage, the torque generated by each electrode will be balanced, and the resultant net force will pull down the mirror vertically (piston motion).

The size of the mirror and the four electrodes are designed to be 500×500×20 μm and 350×350×20 μm, respectively, whereas the universal joint is 80 μm tall with 60 μm diameter. The air gap between the mirror and electrodes is 20 μm. Be noted that the main purpose of this thesis is to demonstrate a new fabrication methodology rather than proposing a device to compete with any preexisting device. Thus, we assume that the current design satisfies the performance requirement. Provided that a specific application is desired, the device design can be further optimized to obtain a more favorable overall performance.

2.2 Analytical Modeling

To model both the static and dynamic behavior of the micromirror device, analytical model is built based on the well-known parallel-plate capacitor model. If we make the assumption that the deflection is small and neglect the fringing electrostatic field, the voltage controlled governing equation for parallel-plate capacitor is given as:

$$F = \frac{1}{2}\frac{\varepsilon A}{d^2}V^2 \tag{2.1}$$

where F is the force between the two electrodes, ε is the permittivity, A is the overlapping area between the electrodes, d is the distance between the plates and V is the applied voltage.

For rectangular parallel-plate capacitor tilting along one of its orthogonal axis, the distance between two plates is not a constant throughout the plate. Nevertheless, we can still get the force acting on an infinitesimal element of the plate following equation (2.1).

$$dA = wdx \tag{2.2a}$$

$$dF = \frac{\varepsilon V^2 dA}{2\left(h - x\sin\theta\right)^2} = \frac{w\varepsilon V^2 dx}{2\left(h - x\sin\theta\right)^2} \tag{2.2b}$$

w is the width of the plate, and the meaning of the other symbols for equation (2.2) can be found in Figure 17 in Appendix A. By integrating the infinitesimal momentum along the length of the plate, we get the applied torque along neutral axis:

$$M(\theta) = \int x dF \cos\theta = \int_{l_1}^{l_2} \cos\theta \frac{w\varepsilon V^2 dx}{2(h - x\sin\theta)^2} \approx \int_{l_1}^{l_2} \frac{w\varepsilon V^2 dx}{2(h - x\theta)^2}$$

$$= \frac{w\varepsilon V^2}{2\theta^2}\left(\frac{h(l_2 - l_1)\theta}{(h - l_2\theta)(h - l_1\theta)} + \ln\frac{h - l_2\theta}{h - l_1\theta}\right) \tag{2.3}$$

From here we can write the equation of motion for the system as equation (2.4), in which *M* (*θ*) follows equation (2.3):

$$I\ddot{\theta} + c\dot{\theta} + k\theta = M(\theta) \tag{2.4}$$

For the static behavior of the mirror system, the equation of motion can be simplified to:

$$k\theta = M(\theta) \tag{2.5a}$$

$$k\theta = \frac{w\varepsilon}{2}\frac{1}{\theta^2}\left(\frac{h(l_2 - l_1)\theta}{(h - l_2\theta)(h - l_1\theta)} + \ln\frac{h - l_2\theta}{h - l_1\theta}\right)V^2 \tag{2.5b}$$

From equation (2.5b), we can see that there is no explicit expression for the static deflection angle θ as a function of the applied voltage *V*. However, we can get an approximate expression by linearization of the torque *M* with respect to angular deflection θ since we made the assumption of small deformation. Refer to appendix A for detailed derivation. With the linearized torque expression we can solve the $\theta(V)$ explicitly as:

$$\theta = \frac{3h\varepsilon w(l_2^2 - l_1^2)V^2}{12h^3k - 4\varepsilon w(l_2^3 - l_1^3)V^2} \tag{2.6}$$

For the dynamic behavior, we can get the resonant frequency from:

$$f_n = \frac{1}{2\pi}\sqrt{\frac{k}{I}} \tag{2.7}$$

Assuming that the beam follows the Euler-Bernoulli cantilever beam theory, the expressions for inertia of moment *I* and stiffness *k* are given as:

$$\begin{aligned} I &= \rho t \frac{w^4}{12} \\ k &= \frac{EI}{l} = \frac{Er^4}{4l} \end{aligned} \tag{2.8}$$

where *l*, *r* are the height and radius of the universal joint, respectively.

Hence, we can approximate the value of resonant frequency as:

$$\begin{aligned} \omega_n &= 2\pi f_n = \sqrt{\frac{k}{I}} = 5741\,(rad/s) \\ f_n &\cong 0.9\,(kHz) \end{aligned} \tag{2.9}$$

It is later shown that the values are not quite true, more than two times smaller than the experimental data. Nevertheless, the analytic model is instrumental for the initial design of the mirror dimensions. The error might come from the implementation of linear beam theory, which may not be quite appropriate in our case since the Euler beam equation is valid only for slender beam under small deformation.

2.3 Finite-Element-Method Modeling

To better predict the dynamic behavior of the system, finite-element-analysis is performed using COMSOL multiphysics 4.3b (Figure. 7). The resonant frequency is obtained by the eigenfrequency analysis module. For simplicity, the Young's modulus of pure PDMS is used in simulation without considering the stiffening effect of CB doping, although this may lead to some underestimation of the resonant frequencies. As a result, six resonant modes with their resonant frequency being 0.79 kHz, 1.43 kHz, 5.58 kHz and 11.8 kHz are captured by the modal analysis. They corresponds to the torsion (z-axis), bending (x and y axes), shearing (x and y axes) and tension (z-axis) deformation of the elastomeric joint. Be aware that two modes exist at 1.43 kHz corresponding to the bending motion along two orthogonal axes. With perfect symmetry, they degenerate to a single mode due to their identical resonant frequencies. Same thing holds for the two shearing modes. Static behavior is also studied and the θ - V curve is later compared with the experimental data.

2.4 Figures

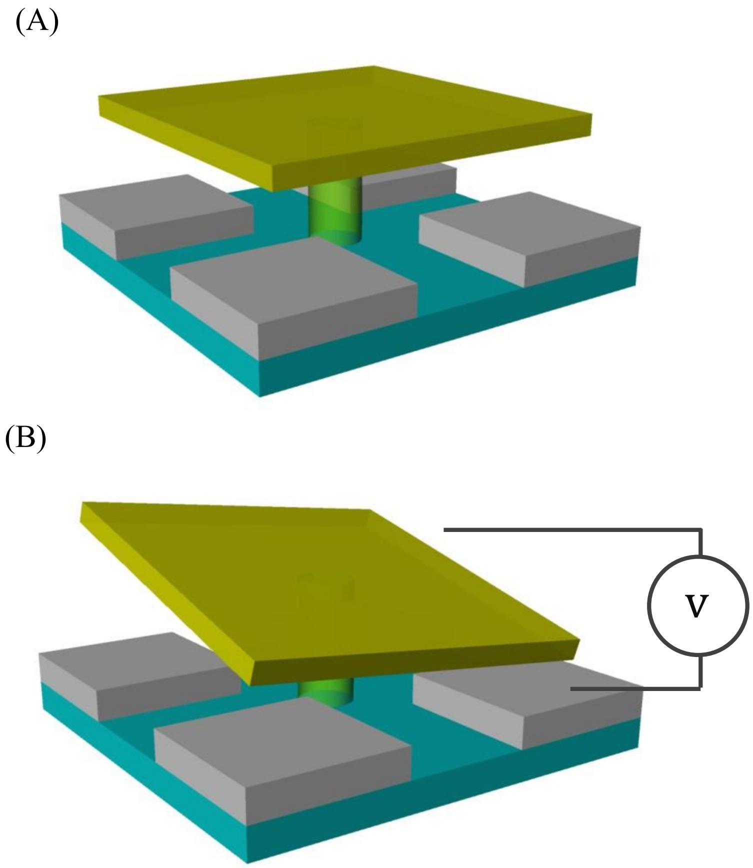

Figure 6. Schematic diagram of the micromirror without actuation (A) and with actuation (B)

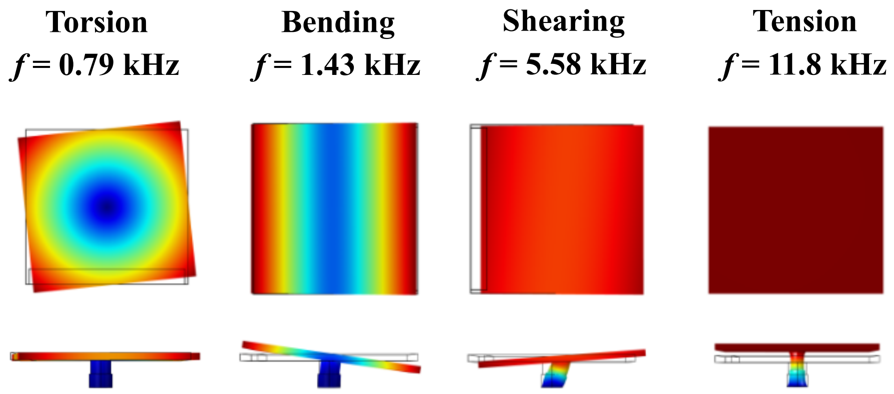

Torsion
f **= 0.79 kHz**

Bending
f **= 1.43 kHz**

Shearing
f **= 5.58 kHz**

Tension
f **= 11.8 kHz**

Figure 7. Finite-element-method modal analysis. The micromirror has four different resonant modes corresponding to the torsion, bending, shearing and tension/compression deformation of the elastomeric universal joint.

Chapter 3: Fabrication

The fabrication process of the micromirror starts with the preparation of donor and receiver substrates. The parts on the donor substrate, what we usually refer to as inks, are eventually assembled on the receiver substrate via a transfer printing process and bonded with a thermal processing step. The overview diagram of the whole process is shown in Figure 8.

3.1 Fabrication of Donor Substrates

Silicon mirrors and electrodes, also referred to as inks, are batch fabricated using monolithic fabrication process on the donor substrate. We use a silicon-on-insulator (SOI) wafer with a 20-μm-thick device layer and a 1-μm-thick buried oxide (BOX) layer here. The full process is summarized below, whereas the representative fabrication steps are depicted in Figure 8 (A1-A3)..

- SOI wafer are cleaned in a piranha solution (sulfuric acid: hydrogen peroxide, 3:1) and patterned through photolithography. The 500×500×20 μm mirrors and the 350×350×20 μm electrodes are patterned on the same 20 μm SOI wafer since they have the same thickness. The wafer is then etched using DRIE by exactly 20 μm, with the 1 μm buried oxide layer (BOX) being a etch stop layer.
- The photoresist is stripped and the wafer is then immersed in hydrofluoric acid solution (49%) for 1 min to etch the BOX layer. Be aware that this wet etching process is isotropic, meaning that the oxide layer underneath the silicon will be undercut for about 1 μm along the edges of silicon structure. Photoresist (AZ5214 E) is again spin-coated flood exposed. While the majority of the photoresist will be removed after development, the photoresist

sitting the in undercut below the silicon will stay intact because UV light cannot expose the photoresist under the silicon. This step is usually termed “anchoring”.

- Finally, the wafer is immersed in hydrofluoric acid (49%) for ~ 3 hours to remove the remaining silicon oxide under the silicon mirrors and electrodes structures. After being successfully released, the silicon “inks” are now free standing except for being tethered by the photoresist anchors around the edge underneath them.

3.2 Fabrication of Receiver Substrates

The fabrication of the receiver substrate is shown in Figure 8 (B1-B3). A three-layer SU-8 mold is patterned by photolithography, followed by silanization to help demolding (Figure. 8 (B1)). Carbon black particles are then selectively deposited and PDMS is cured on the mold.

The negative mold is made by photolithographically pattern SU-8 50 epoxy on a single side polished silicon wafer (Figure 9). As a first step, a single side polished (SSP) wafer is thoroughly cleaned by RCA cleaning and baked on a 150℃ hotplate for 5 min to dehydrate the wafer surface. This step guarantees good adhesion between the silicon and SU-8 epoxy since the SU-8 epoxy will remain on the wafer as permanent structures of the mold. SU-8 50 negative photoresist is used because it gives the right thickness with good consistency (40 μm at a spin speed of 3000 rpm). The first layer defines a cylindrical cavity, which corresponds to the top part of the universal joint. After spin-coating the first layer of SU-8 photoresist, the wafer is soft-baked and exposure to a dose of 400 mJ/cm^2. After post exposure bake and development, the SU-8 sidewall exhibits a slightly positive slope. This is favorable because the SU-8 structures will be used as part of the negative mold so the positive sidewall makes the demold process easier. Similar photolithography processes are repeated twice to define the second and third layer, from which the electrodes and interconnects will be formed. The SU-8 structures are hard-baked at 150℃ for 5min before any other treatment to make it a permanent structure on the silicon wafer. Anti-stick coating is then performed at room temperature by evaporating trichlorosilane along with the molds in a vacuum jar to create a nonstick surface leading to better demold.

The mold can be used for PDMS molding right after the silanization. However, conductive carbon black (CB) particles need to be applied into the trench of the negative mold first in order to embed conductive carbon black particles those regions. To start with, carbon black powder are mixed with toluene and agitated with magnetic stirrer for 1 day. The resultant CB/toluene dispersion is applied atop the surface of the mold. After fully evaporation of toluene, the entire mold surface is left coated with carbon black particles uniformly. Excessive CB particles on the very top surface are then removed by commercial pressure sensitive tapes such that only the surface of the trenches remains coated with CB particles (Figure. 8 (B2)). Finally, well-mixed 10:1 PDMS precursor is poured onto the mold and partially cured at 60 °C for 30 min. After demold, PDMS substrate with conductive PDMS regions on a non-conductive PDMS backing layer is mounted on a glass slide and the receiver substrate is ready to use.

3.3 Microassembly Process

The retrievable silicon components on the donor substrate, i.e., top mirrors and bottom electrodes, needs to be transferred to the partially cured CB-PDMS receiver substrate promptly after the partial curing. Upon completion of the pick-and-place procedure, the paused thermal curing of PDMS is resumed and the components are permanently bonded together at 60 °C for ~12h (Figure 8 (A3, C1)).

A deterministic transfer printing technique using elastomeric microtip stamp was employed in this work to retrieve the silicon components from the donor substrate and place them on the receiver substrate (Figure 8). The geometry of the stamp consists of a ~1mm thick backing layer, a 400×400×100 μm cubic post and an array of 15-μm-wide pyramidal relief on the surface of the stamp. The fabrication process of the stamp is depicted in Figure 9. The fabrication flow starts with deposition of a 100nm-thick silicon nitride layer on silicon (100) wafer via Plasma-enhanced-chemical-vapor-deposition (PECVD). The nitride masking layer is then patterned by photolithography and RIE to generate an array of square opening. Wet etching using potassium hydroxide solution (KOH, 30% concentration) is performed to etch the silicon along (111) crystalline plane. This anisotropic etching step defines the pyramidal-shaped relief on the stamp surface. SU-8 50 photoresist is coated and photolithographically patterned to form a square cavity on the mold, which defines the 400×400×100 μm cubic post. After anti-stick coating to the mold, PDMS precursor with 5:1 mixing ratio is cast as the elastomeric stamp material. After fully curing for prolonged time and demolding, the PDMS stamp is mounted on a stamping machine with high precision mechanical stage and optics.

The transfer printing process mainly involves three steps: picking-up, manipulation and printing. Firstly, the stamp is moved to the desired location atop the donor substrate and made full contact with the silicon ink. The pyramidal-shape elastomer microtips have small rigidity so that they collapse upon loading during the initial contact. The actually contact area is almost 100% that of the ink area owing to the collapse of stamp. This state is called “adhesion-on” state. Rapid retrieval of the stamp peels the ink from the donor substrate, leaving the photoresist anchor fractured at the same time. The adhesion between the ink and the stamp is further enhanced by the viscoelastic behavior of elastomer during rapid retrieval since the adhesion of the elastomer stamp is rate dependent [10]. Right after pick-up, the store strain energy in the microtips makes the stamp deform to its original shape and the contact point between the ink and the stamp are now merely the small areas at the tips of the pyramids. This state is called "adhesion-off" state. The ink, either a mirror or an electrode, can then be manipulated to the desired location on the receiver substrate. Usually, printing silicon components on a rigid receiver surface such as silicon wafer requires slow retrieval to minimize the adhesion between the stamp and the ink. However, printing takes place much easier in our case because the receiver substrate is partially cured PDMS (10:1 mixing ratio), which is stickier than the PDMS stamp (5:1 mixing ratio). Furthermore, the contact area between the flat receiver substrate and silicon ink is much larger than the contact area between the microtip stamp and silicon ink. For these reasons, printing turned out to be fairly easy. The resolution of the transfer printing process is mainly determined by the condition of the stage and optics. In our case the resolution is about 5 μm.

Four electrodes and one single crystal mirror are transfer printed on the partially cured CB-PDMS receiver substrate in a sequential manner to form a single mirror. After finishing all the transfer printing steps, the assembly is placed in an oven at 60 °C for 12 hour to assure a fully curing. During the curing, irreversible bonding is achieved through hydroxyl condensation reactions. It is later discovered that both mechanical and electrical interconnection are formed after the final binding step (chapter 4.4).

3.4 Figures

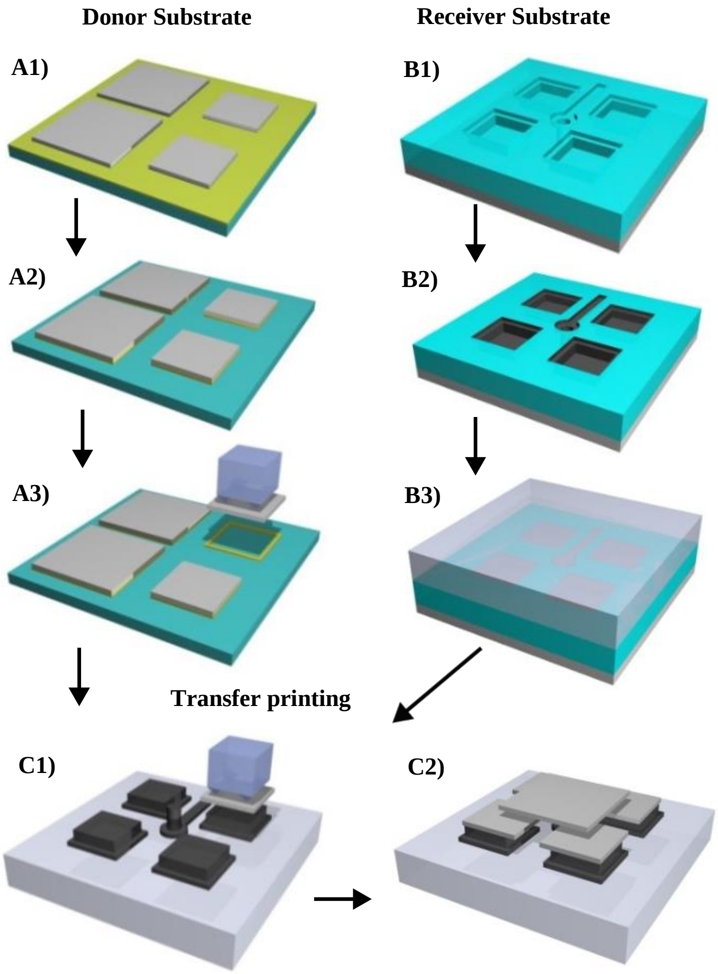

Figure 8. *Fabrication of a silicon donor substrate*: (A1) Etch the device layer of an SOI wafer; (A2) Undercut a BOX layer and pattern photoresist anchors; (A3) Etch away the remaining BOX layer by HF and the silicon components are ready to be retrieved. *Fabrication of a PDMS receiver substrate*: (B1) Pattern an SU8 mold by photolithography; (B2) Selectively deposit CB particles; (B3) Pour and partially cure PDMS to get the receiver substrate. *Assembly between silicon and PDMS parts*: (C1) Retrieve the silicon components from the donor substrate using a microtip stamp and place them on the PDMS receiver substrate; (C2) Fully cure PDMS to bond the silicon and PDMS parts together.

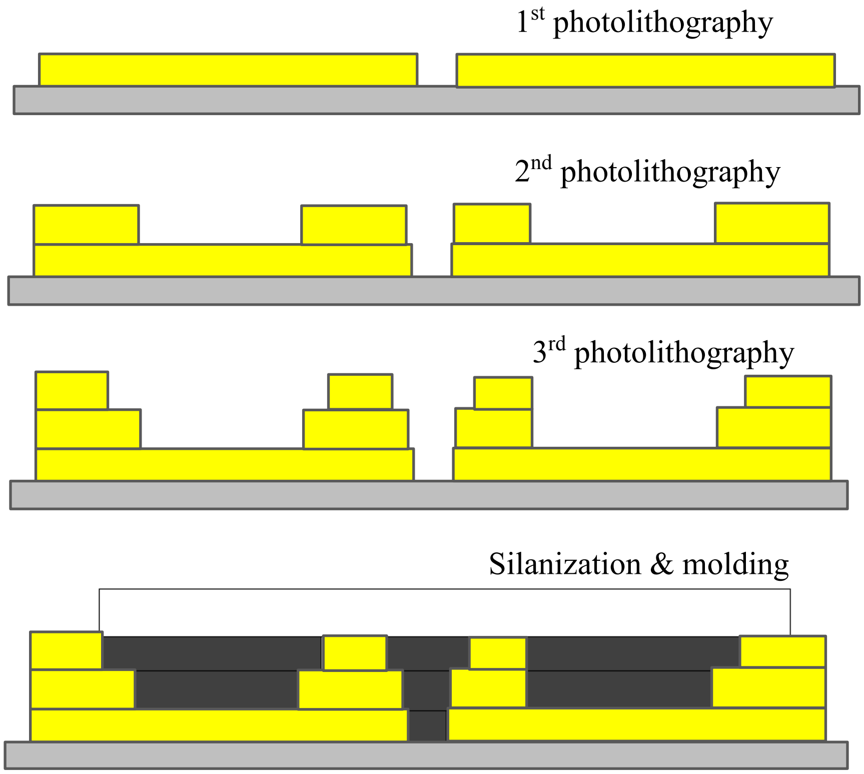

Figure 9. Fabrication flow of the SU-8 mold and PDMS molding process.

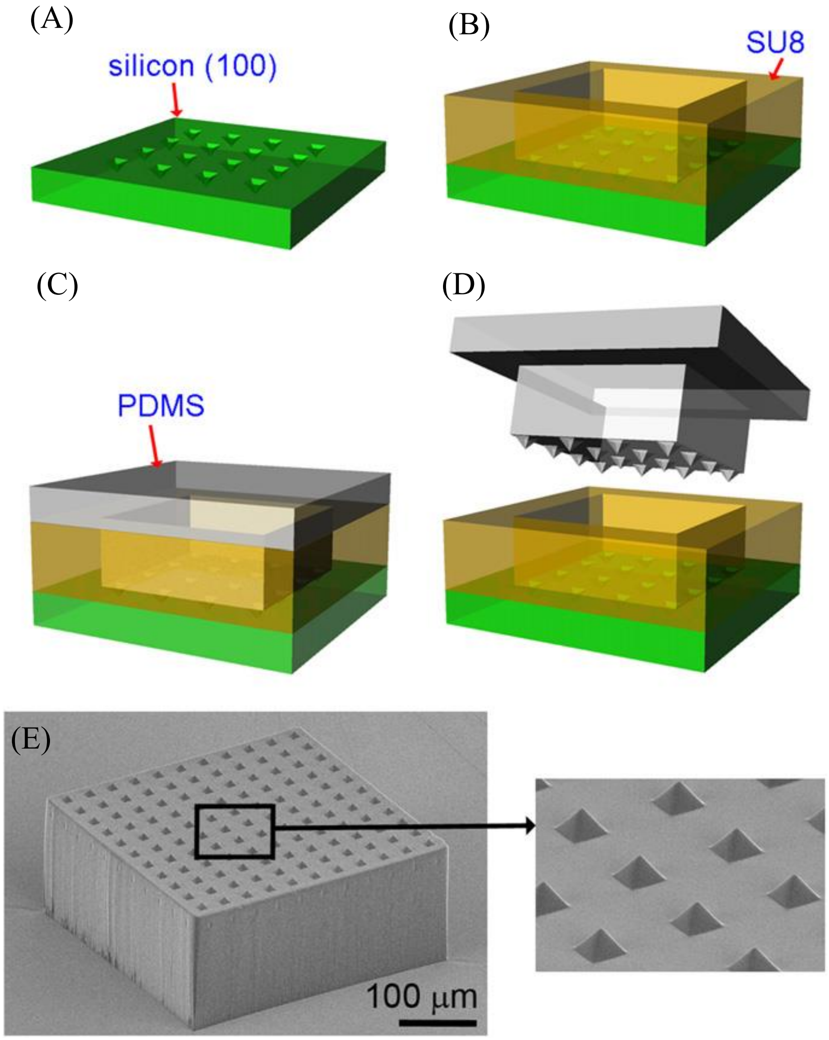

Figure 10. Microtip stamp fabrication process. (A) Formation of multiple pits using KOH etching on a silicon (100) wafer, (B) SU 8 pattern, (C) PDMS molding, (D) PDMS demolding after curing. (E) The SEM image of a fabricated microtipped stamp with its magnified view in the right frame. [10]

Chapter 4: Characterization

The scanning electron microscopy (SEM) images of the fabricated device are shown in Figure 11. The structure of the universal joint can be clearly viewed. To characterize the performance of the device as a micromirror, static and dynamic deflection of the device is tested.

4.1 Static Behavior Characterization

The static behavior of the micromirror is characterized by applying DC voltage to the device and measuring the resultant deflection using an optical profiler (NT1000, Veeco). In order to apply voltage to the devices, the microfabricated samples are mounted on a custom-made printed circuit board (PCB). The Veeco optical profiler will measure the 3D profile of the surface. The instantaneous deflection angle can be calculated by measuring the height difference between the two edges of the mirror. The results for both x and y-axis rotation and z-axis piston are shown in Figure 12. Due to its symmetric shape, the micromirror exhibits almost identical DC Characteristics about x and y axes. Snap-down occurs under a DC voltage of 25 V. The snap-down voltage is relatively low, mainly due to the fact that the air gap between top mirror and bottom electrodes is only 20 μm. The piston stroke is measured by applying the same voltage to the four electrodes at the same time. The uniform attractive force acting between the mirror and the electrodes will cause a compression of the universal joint and therefore a piston motion of the mirror. A piston stroke of 2 μm is observed other 30V.

4.2 Dynamic Behavior Characterization

The frequency response of the devices is also characterized, as shown in Figure 13. A sinusoidal voltage signal with an offset expressed as $V(t) = 5\sin(2\pi f_{act} t) + 5$ is applied to actuate the mirror along the x or y-axis. A collimated laser is directed onto the mirror and the length of its reflected pattern is measured under different driving frequencies as shown in Figure 13 (B). The deflection angles are calculated based on trigonometry. The experimental data is fitted to Lorentzian function, which exhibits a good match. The resonant frequency of the x and y-axis is then determined to be 1.87 kHz and 1.86 kHz, respectively. The quality factor for both x and y-axis is determined to be 1.8. Note that the measured resonant frequencies are larger than the predicted values, probably due to the aforementioned underestimation for the Young's modulus of CB-PDMS. The resonant frequency of the x and y-axis matches each other due to the symmetric geometry of the micromirror. When different scanning frequencies along x and y-axis are need, we can easily break the symmetry of the device by changing the design of the joint and the mirror.

4.3 Mechanical Stiffness Measurement of Universal Joint

The spring constant of the elastomeric universal joint for its piston stroke is characterized to be 42.4 N/m using nano-indentation (TI-950 Triboindenter, Hysitron). The force-displacement curve for angular deflection is measured by poking the tip of nanoindentor around the edge of the mirror, which is shown in Figure 14. Two universal joints made from pure PDMS and CB-PDMS are measured under the same condition to compare the effect of carbon black inclusions. Surprising, the stiffness of CB-PDMS composite universal joint is only slightly larger compared to the pure PDMS one. This result can be explained by the non-uniform distribution of carbon black particles in the PDMS matrix. After the carbon black deposition process, it can be seen from microscopic inspection that the carbon black particles did not fill the trench completely. We assume that the carbon black particles reside on the mold only at the surface level, leading to the decomposed mechanical and electrical property of the joint. In other word, the CB-PDMS universal joints exhibit high electrical conductivity as part of its surface property whereas the mechanical behavior is still a bulk property which is similar to pure PDMS. In general, this phenomenon is favorable because we can obtain reliable electrical interconnection without increasing the stiffness of the universal joint extensively.

4.4 Contact Resistance Measurement of Silicon/CB-PDMS Interface

To realize electrostatic actuation, the mirror has to be electrically interconnected to the universal joint and the electrodes have to be electrically interconnected to the base underneath them. To characterize the quality of this interconnection, we measure the interfacial resistance between the silicon and CB-PDMS material by a testing approach inspired by transmission line measurement (Figure 15). Specimens with five CB-PDMS strips are prepared by the molding process similar to what we used for actual mirror device. The five CB-PDMS strips one the same specimen have the same width and thickness but different length. For each strip, the width is 350 μm and the height is 40 μm, whereas the length varies from 1.05 mm to 2.45 mm. After molding, highly doped silicon electrodes are transfer-printed on each ends of every strip. By probing on the silicon electrodes and measuring the I-V curve for every strip using a probe station, five data points can be obtained from each specimen (Figure 16). Linear regression of the data points gives the contact resistance and sheet resistance value (CB-PDMS) following the equation (3.1):

$$R_T = 2R_C + \frac{R_{SH} d}{w} \tag{3.1}$$

The interfacial contact resistance between doped silicon electrodes and the CB-PDMS strip is one half of the intercept value, which is determined to be 5 kΩ. We can also get the sheet resistance of CB-PDMS strip which is 17 kΩ/□. The absolute numbers do not mean too much, but the orders of magnitude suggest that the interfacial contact resistance is low enough to support electrostatic actuation.

4.5 Figures

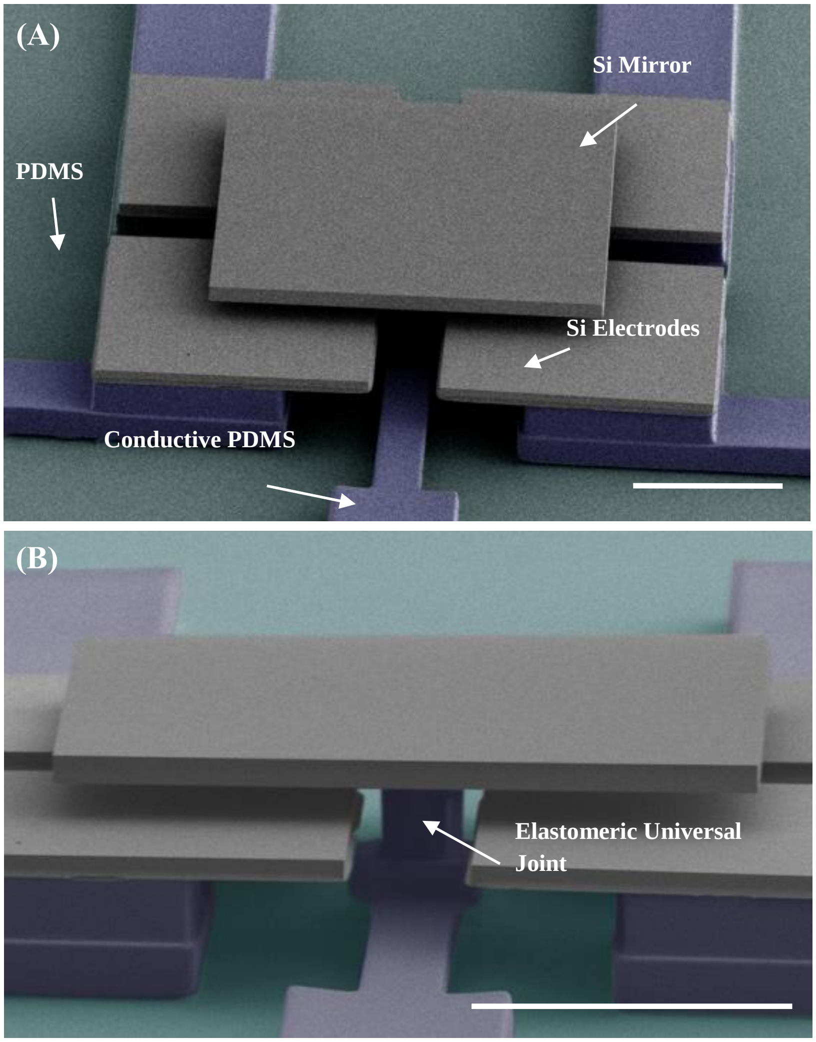

Figure 11. Colored SEM images of the micromirror. (A) The assembled device is composed of a top mirror and four bottom electrodes. (B) The image shows the side view of the elastomeric universal joint. Scale bars are 200 μm.

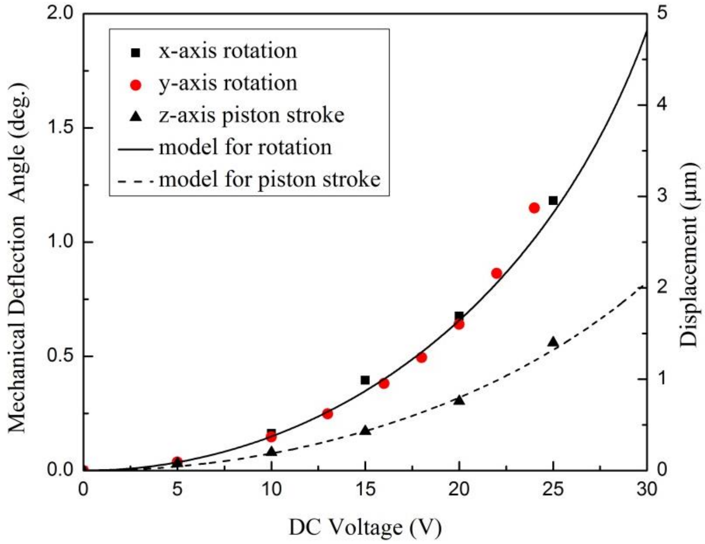

Figure 12. DC characteristics of the micromirror for x-axis rotation, y-axis rotation and compressive piston motion.

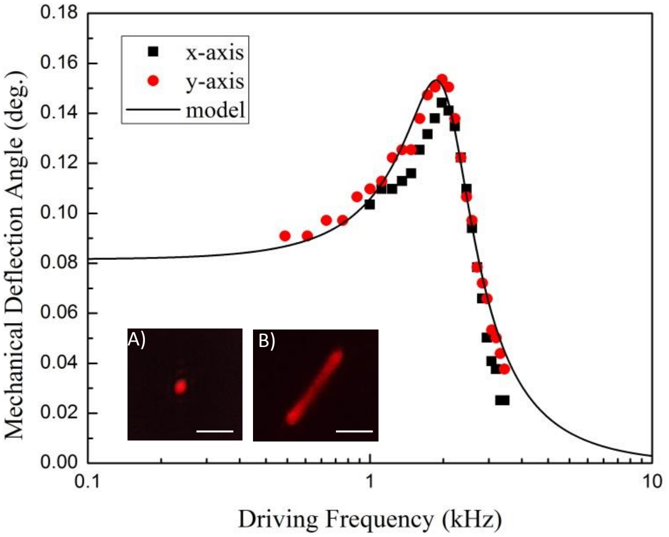

Figure 13 Frequency response for x and y axis rotation. The resonant frequency is ~ 1.8 kHz for both axes. Inset images show the laser scanning trajectory at 0 Hz (A) and 1.8 kHz (B). Scale bars are 1cm.

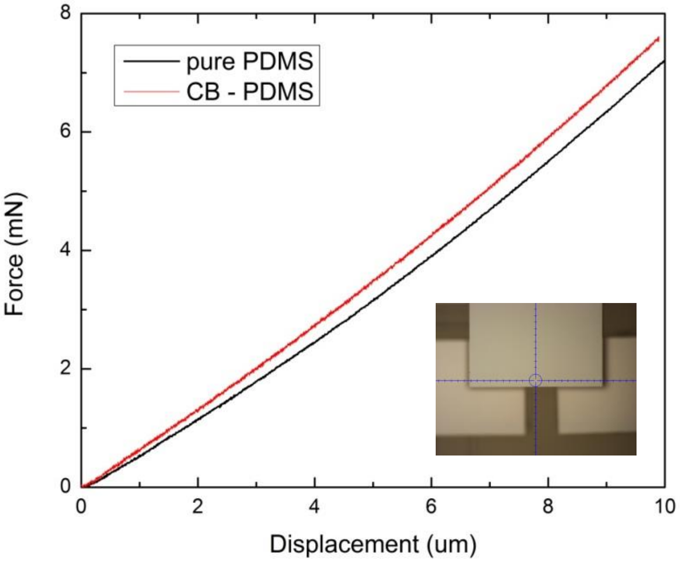

Figure 14. Nanoindentation testing results. The inset shows the location of indentation.

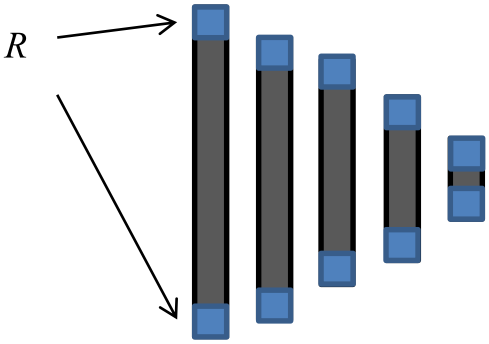

Figure 15. Schematic diagram of the contact resistance measurement specimen.

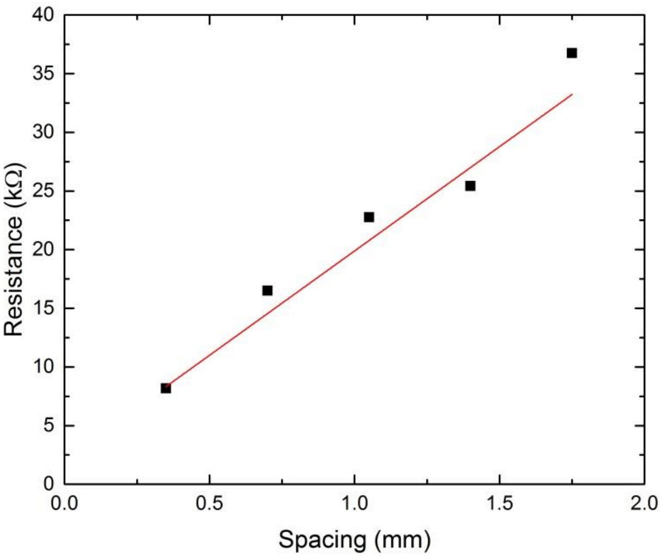

Figure 16. results of CB-PDMS/silicon interface contact resistance measurement.

Chapter 5: Conclusion

While conventional silicon based micromirrors have brought impact to the modern technologies, there are certain limits to their performance. This thesis sets out to find a the design, fabrication and characterization method to obtain a hybrid micromirror untilizing a elastomeric universal joint structure. The scope of current work focus on the fabrication method to create elastomer and silicon heterogeous structure: CB-PDMS is used as the deformable universal joint to take the advantage its flexibility and high conductivity whereas single crystal silicon mirror provides high quality optical reflective surface. The performance of the devices is characterized, including the static and dynamic behavior characterization.

5.1 Recommended Future Studies

One immediate future work is to adopt the methodology presented in this paper to other designs of micromirror devices with specified application. An ongoing work is to design a two-axis scanning mirror with ~ 1mm diameter and larger scanning angle ~5℃. The two-axis scanner can be used as one of the key component in optical coherent tomography endoscope. To increase the reflectivity of the mirror, Au layer will be deposited on the mirror. The shape of the mirror will likely to be circular to better reflect the laser beam.

Besides micromirror applications, our methodology to create elastomer-based hybrid structures can be readily extended to other MEMS devices. One of the promising devices is MEMS energy harvester utilizing elastomer as the flexure springs and other high density metals (such as nickel) as the proof mass. The hybrid device will likely to increase the energy harvesting efficiency due to the low rigidity of springs.

The main limitation of the current work is the challenge in terms of electrical interconnection. Since the soft PDMS is used as the substrate material, the well-developed wire bonding technique does not work well in the same way as for silicon substrate. As a result, the packing density is limited, which makes our current version of devices unsuitable for applications that require high density arrays of mirrors. However, this limitation can be break down if we developed a method to address the devices in a more efficient manner.

References

[1]. N. Maluf, K. Williams, An Introduction to Microeletromechaincal Systems Engineering. Boston & London: Artech House, 2004

[2]. P.F. Van Kessel, L. J. Hornbeck, R. E. Meier, and M. R. Douglass, “A MEMS-Based Projection Display”, *Proc. of The IEEE,* Vol. 86, No. 8, August 1998

[3]. Jui-che Tsai and Ming C. Wu, “Gimbal-Less MEMS Two-Axis Optical Scanner Array With High Fill-Factor”, *Journal of Microelectromechanical Systems,* Vol. 14, No. 6, December 2005

[4]. K. Aljasem, L. Froehly, A. Seifert, and H. Zappe, “Scanning and Tunable Micro-Optics for Endoscopic Optical Coherence Tomography”, *Journal of Microelectromechanical Systems,* Vol. 20, No. 6, December 2011

[5]. V. Milanovic, G. A. Matus, and D. T. McCormick, “Gimbal-Less Monolithic Silicon actuators for Tip–Tilt–Piston Micromirror Applications ”, *IEEE Journal of Selected Topics In Quantum Electronics,* Vol. 10, No. 3, May/June 2004

[6]. https://www.mems.sandia.gov/samples/doc/SUMMiT_V_Dmanual.pdf

[7]. http://www.memscap.com/__data/assets/pdf_file/0019/1774/SOIMUMPs.dr.v8.0.pdf

[8]. Y. Tung, and K. Kurabayashi, “A Single-Layer PDMS-on-Silicon Hybrid Microactuator with Multi-Axis Out-of-Plane Motion Capabilities—Part I: Design and Analysis”, *Journal of Microelectromechanical Systems*, Vol. 14, No. 3, June 2005

[9]. C. Liu, “Recent Developments in Polymer MEMS”, Adv. Mater. 2007, 19, 3783–3790

[10]. H. Keum, A. Carlson, H. Ning, A. Mihi, J. D. Eisenhaure, P. V. Braun, J. A. Rogers and S. Kim, “Silicon micro-masonry using elastomeric stamps for three-dimensional microfabrication”, *Journal of Micromechanics and Microengineering,* 22 (2012) 055018 (7pp)

[11]. Y. Zhang, H. Keum, K. Park, R. Bashir, and S. Kim, “Micro-Masonry of MEMS Sensors and Actuators”, *Journal of Microelectromechanical Systems*, Vol. 23, No. 2, April 2014

Appendix A: Linearization of Electrostatic Torque

We have the expression for net moment as:

$$M = \frac{w\varepsilon V^2}{2\theta^2}\left(\frac{h\left(l_2 - l_1\right)\theta}{\left(h - l_2\theta\right)\left(h - l_1\theta\right)} + \ln\frac{h - l_2\theta}{h - l_1\theta}\right) \qquad \text{(A. 1)}$$

Approximating the net moment by Taylor series leads to

$$\begin{aligned} &M = \alpha_0 V^2 + \alpha_1 V^2\theta + \alpha_2 V^2\theta^2 + \alpha_3 V^2\theta^3 \\ &\alpha_0 = \frac{\varepsilon w(l_2^2 - l_1^2)}{4h^2} \\ &\alpha_1 = \frac{\varepsilon w(l_2^3 - l_1^3)}{3h^3} \\ &\alpha_2 = \frac{3\varepsilon w(l_2^4 - l_1^4)}{8h^3} \\ &\alpha_4 = \frac{2\varepsilon w(l_2^5 - l_1^5)}{5h^3} \end{aligned} \qquad \text{(A.2)}$$

The applied voltage is a harmonic function of time, whose expression is given as:

$$V(t) = V_{ac}\cos\omega t + V_{dc} \qquad \text{(A. 3a)}$$

Thus, the square of *V* has the expression:

$$\begin{aligned} &V^2(t) \\ &= V_{ac}{}^2\cos^2\omega t + 2V_{dc}V_{ac}\cos\omega t + V_{dc}{}^2 \\ &= \frac{V_{ac}{}^2}{2}\left(1 + \cos 2\omega t\right) + 2V_{dc}V_{ac}\cos\omega t + V_{dc}{}^2 \\ &= \frac{V_{ac}{}^2}{2}\cos 2\omega t + 2V_{dc}V_{ac}\cos\omega t + V_{dc}{}^2 + \frac{V_{ac}{}^2}{2} \end{aligned} \qquad \text{(A. 3b)}$$

Hence, a linearized torque can be expressed as:

$$M \cong \alpha_0 V^2 + \alpha_1 V^2\theta \qquad \text{(A. 4)}$$

Equation of motion for static case is written as:

$$k\theta = M\left(\theta\right) \tag{A. 5}$$

Substitute equation (A. 2) into it, we get the relation between angular deflection and applied voltage as:

$$\theta = \frac{3h\varepsilon w(l_2^2 - l_1^2)V^2}{12h^3k - 4\varepsilon w(l_2^3 - l_1^3)V^2} \tag{A.6}$$

which is equation (2.6).

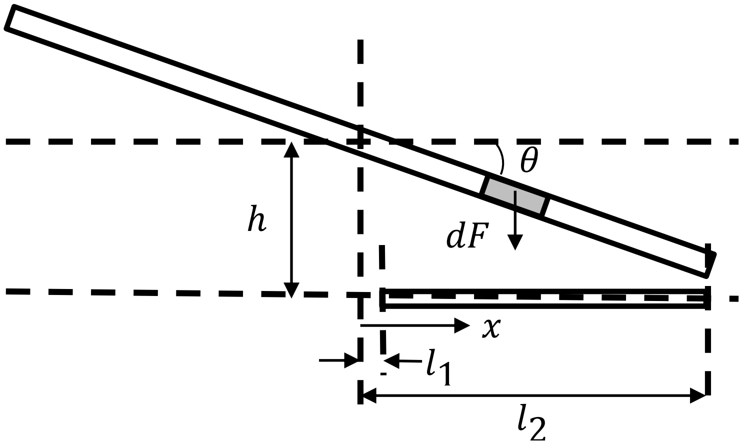

Figure 17. Schematic view of tilting mirror model.